

A Search for UHE Tau Neutrinos with IceCube

R. Abbasi,²⁸ Y. Abdou,²³ T. Abu-Zayyad,³⁴ M. Ackermann,⁴² J. Adams,¹⁶ J. A. Aguilar,²² M. Ahlers,²⁸ D. Altmann,¹ K. Andeen,²⁸ J. Auffenberg,²⁸ X. Bai,^{32,*} M. Baker,²⁸ S. W. Barwick,²⁴ V. Baum,²⁹ R. Bay,⁷ K. Beattie,⁸ J. J. Beatty,^{18,19} S. Bechet,¹³ J. K. Becker,¹⁰ K.-H. Becker,⁴¹ M. Bell,³⁹ M. L. Benabderrahmane,⁴² S. BenZvi,²⁸ J. Berdermann,⁴² P. Berghaus,³² D. Berley,¹⁷ E. Bernardini,⁴² D. Bertrand,¹³ D. Z. Besson,²⁶ D. Bindig,⁴¹ M. Bissok,¹ E. Blaufuss,¹⁷ J. Blumenthal,¹ D. J. Boersma,¹ C. Bohm,³⁵ D. Bose,¹⁴ S. Böser,¹¹ O. Botner,⁴⁰ L. Brayeur,¹⁴ A. M. Brown,¹⁶ S. Buitink,¹⁴ K. S. Caballero-Mora,³⁹ M. Carson,²³ M. Casier,¹⁴ D. Chirkin,²⁸ B. Christy,¹⁷ F. Clevermann,²⁰ S. Cohen,²⁵ D. F. Cowen,^{39,38} A. H. Cruz Silva,⁴² M. V. D'Agostino,⁷ M. Danninger,³⁵ J. Daughhetee,⁵ J. C. Davis,¹⁸ C. De Clercq,¹⁴ T. Degner,¹¹ F. Descamps,²³ P. Desiati,²⁸ G. de Vries-Uiterweerd,²³ T. DeYoung,³⁹ J. C. Díaz-Vélez,²⁸ J. Dreyer,¹⁰ J. P. Dumm,²⁸ M. Dunkman,³⁹ J. Eisch,²⁸ R. W. Ellsworth,¹⁷ O. Engdegård,⁴⁰ S. Euler,¹ P. A. Evenson,³² O. Fadiran,²⁸ A. R. Fazely,⁶ A. Fedynitch,¹⁰ J. Feintzeig,²⁸ T. Feusels,²³ K. Filimonov,⁷ C. Finley,³⁵ T. Fischer-Wasels,⁴¹ S. Flis,³⁵ A. Franckowiak,¹¹ R. Franke,⁴² T. K. Gaisser,³² J. Gallagher,²⁷ L. Gerhardt,^{8,7} L. Gladstone,²⁸ T. Glüsenkamp,⁴² A. Goldschmidt,⁸ J. A. Goodman,¹⁷ D. Góra,⁴² D. Grant,²¹ A. Groß,³¹ S. Grullon,²⁸ M. Gurtner,⁴¹ C. Ha,^{8,7} A. Haj Ismail,²³ A. Hallgren,⁴⁰ F. Halzen,²⁸ K. Hanson,¹³ D. Heereman,¹³ P. Heimann,¹ D. Heinen,¹ K. Helbing,⁴¹ R. Hellauer,¹⁷ S. Hickford,¹⁶ G. C. Hill,² K. D. Hoffman,¹⁷ B. Hoffmann,¹ A. Homeier,¹¹ K. Hoshina,²⁸ W. Huelsnitz,^{17,†} P. O. Hulth,³⁵ K. Hultqvist,³⁵ S. Hussain,³² A. Ishihara,¹⁵ E. Jacobi,⁴² J. Jacobsen,²⁸ G. S. Japaridze,⁴ H. Johansson,³⁵ A. Kappes,⁹ T. Karg,⁴¹ A. Karle,²⁸ J. Kiryluk,³⁶ F. Kislak,⁴² S. R. Klein,^{8,7} J.-H. Köhne,²⁰ G. Kohnen,³⁰ H. Kolanoski,⁹ L. Köpke,²⁹ S. Kopper,⁴¹ D. J. Koskinen,³⁹ M. Kowalski,¹¹ M. Krasberg,²⁸ G. Kroll,²⁹ J. Kunnen,¹⁴ N. Kurahashi,²⁸ T. Kuwabara,³² M. Labare,¹⁴ K. Laihem,¹ H. Landsman,²⁸ M. J. Larson,³⁹ R. Lauer,⁴² J. Lünemann,²⁹ J. Madsen,³⁴ R. Maruyama,²⁸ K. Mase,¹⁵ H. S. Matis,⁸ K. Meagher,¹⁷ M. Merck,²⁸ P. Mészáros,^{38,39} T. Meures,¹³ S. Miarecki,^{8,7} E. Middell,⁴² N. Milke,²⁰ J. Miller,¹⁴ T. Montaruli,^{22,‡} R. Morse,²⁸ S. M. Movit,³⁸ R. Nahnhauser,⁴² J. W. Nam,²⁴ U. Naumann,⁴¹ S. C. Nowicki,²¹ D. R. Nygren,⁸ S. Odrowski,³¹ A. Olivas,¹⁷ M. Olivo,¹⁰ A. O'Murchadha,²⁸ S. Panknin,¹¹ L. Paul,¹ C. Pérez de los Heros,⁴⁰ D. Pieloth,²⁰ J. Posselt,⁴¹ P. B. Price,⁷ G. T. Przybylski,⁸ K. Rawlins,³ P. Redl,¹⁷ E. Resconi,³¹ W. Rhode,²⁰ M. Ribordy,²⁵ M. Richman,¹⁷ B. Riedel,²⁸ J. P. Rodrigues,²⁸ F. Rothmaier,²⁹ C. Rott,¹⁸ T. Ruhe,²⁰ D. Rutledge,³⁹ B. Ruzybayev,³² D. Ryckbosch,²³ H.-G. Sander,²⁹ M. Santander,²⁸ S. Sarkar,³³ K. Schatto,²⁹ M. Scheel,¹ T. Schmidt,¹⁷ S. Schöneberg,¹⁰ A. Schönwald,⁴² A. Schukraft,¹ L. Schulte,¹¹ A. Schultes,⁴¹ O. Schulz,³¹ M. Schunck,¹ D. Seckel,³² B. Semburg,⁴¹ S. H. Seo,^{35,§} Y. Sestayo,³¹ S. Seunarine,¹² A. Silvestri,²⁴ M. W. E. Smith,³⁹ G. M. Spiczak,³⁴ C. Spiering,⁴² M. Stamatikos,^{18,¶} T. Stanev,³² T. Stezelberger,⁸ R. G. Stokstad,⁸ A. Stöbl,⁴² E. A. Strahler,¹⁴ R. Ström,⁴⁰ M. Stüer,¹¹ G. W. Sullivan,¹⁷ H. Taavola,⁴⁰ I. Taboada,⁵ A. Tamburro,³² S. Ter-Antonyan,⁶ S. Tilav,³² P. A. Toale,³⁷ S. Toscano,²⁸ N. van Eijndhoven,¹⁴ A. Van Overloop,²³ J. van Santen,²⁸ M. Vehring,¹ M. Voge,¹¹ C. Walck,³⁵ T. Waldenmaier,⁹ M. Wallraff,¹ M. Walter,⁴² R. Wasserman,³⁹ Ch. Weaver,²⁸ C. Wendt,²⁸ S. Westerhoff,²⁸ N. Whitehorn,²⁸ K. Wiebe,²⁹ C. H. Wiebusch,¹ D. R. Williams,³⁷ R. Wischniewski,⁴² H. Wissing,¹⁷ M. Wolf,³⁵ T. R. Wood,²¹ K. Woschnagg,⁷ C. Xu,³² D. L. Xu,³⁷ X. W. Xu,⁶ J. P. Yanez,⁴² G. Yodh,²⁴ S. Yoshida,¹⁵ P. Zarzhitsky,³⁷ and M. Zoll³⁵

(IceCube Collaboration)

¹III. Physikalisches Institut, RWTH Aachen University, D-52056 Aachen, Germany

²School of Chemistry & Physics, University of Adelaide, Adelaide SA, 5005 Australia

³Dept. of Physics and Astronomy, University of Alaska Anchorage,
3211 Providence Dr., Anchorage, AK 99508, USA

⁴CTSPS, Clark-Atlanta University, Atlanta, GA 30314, USA

⁵School of Physics and Center for Relativistic Astrophysics,
Georgia Institute of Technology, Atlanta, GA 30332, USA

⁶Dept. of Physics, Southern University, Baton Rouge, LA 70813, USA

⁷Dept. of Physics, University of California, Berkeley, CA 94720, USA

⁸Lawrence Berkeley National Laboratory, Berkeley, CA 94720, USA

⁹Institut für Physik, Humboldt-Universität zu Berlin, D-12489 Berlin, Germany

¹⁰Fakultät für Physik & Astronomie, Ruhr-Universität Bochum, D-44780 Bochum, Germany

¹¹Physikalisches Institut, Universität Bonn, Nussallee 12, D-53115 Bonn, Germany

¹²Dept. of Physics, University of the West Indies,
Cave Hill Campus, Bridgetown BB11000, Barbados

¹³Université Libre de Bruxelles, Science Faculty CP230, B-1050 Brussels, Belgium

¹⁴Vrije Universiteit Brussel, Dienst ELEM, B-1050 Brussels, Belgium

¹⁵Dept. of Physics, Chiba University, Chiba 263-8522, Japan

- ¹⁶Dept. of Physics and Astronomy, University of Canterbury, Private Bag 4800, Christchurch, New Zealand
¹⁷Dept. of Physics, University of Maryland, College Park, MD 20742, USA
¹⁸Dept. of Physics and Center for Cosmology and Astro-Particle Physics, Ohio State University, Columbus, OH 43210, USA
¹⁹Dept. of Astronomy, Ohio State University, Columbus, OH 43210, USA
²⁰Dept. of Physics, TU Dortmund University, D-44221 Dortmund, Germany
²¹Dept. of Physics, University of Alberta, Edmonton, Alberta, Canada T6G 2G7
²²Département de physique nucléaire et corpusculaire, Université de Genève, CH-1211 Genève, Switzerland
²³Dept. of Physics and Astronomy, University of Gent, B-9000 Gent, Belgium
²⁴Dept. of Physics and Astronomy, University of California, Irvine, CA 92697, USA
²⁵Laboratory for High Energy Physics, École Polytechnique Fédérale, CH-1015 Lausanne, Switzerland
²⁶Dept. of Physics and Astronomy, University of Kansas, Lawrence, KS 66045, USA
²⁷Dept. of Astronomy, University of Wisconsin, Madison, WI 53706, USA
²⁸Dept. of Physics, University of Wisconsin, Madison, WI 53706, USA
²⁹Institute of Physics, University of Mainz, Staudinger Weg 7, D-55099 Mainz, Germany
³⁰Université de Mons, 7000 Mons, Belgium
³¹T.U. Munich, D-85748 Garching, Germany
³²Bartol Research Institute and Department of Physics and Astronomy, University of Delaware, Newark, DE 19716, USA
³³Dept. of Physics, University of Oxford, 1 Keble Road, Oxford OX1 3NP, UK
³⁴Dept. of Physics, University of Wisconsin, River Falls, WI 54022, USA
³⁵Oskar Klein Centre and Dept. of Physics, Stockholm University, SE-10691 Stockholm, Sweden
³⁶Department of Physics and Astronomy, Stony Brook University, Stony Brook, NY 11794-3800, USA
³⁷Dept. of Physics and Astronomy, University of Alabama, Tuscaloosa, AL 35487, USA
³⁸Dept. of Astronomy and Astrophysics, Pennsylvania State University, University Park, PA 16802, USA
³⁹Dept. of Physics, Pennsylvania State University, University Park, PA 16802, USA
⁴⁰Dept. of Physics and Astronomy, Uppsala University, Box 516, S-75120 Uppsala, Sweden
⁴¹Dept. of Physics, University of Wuppertal, D-42119 Wuppertal, Germany
⁴²DESY, D-15735 Zeuthen, Germany
- (Dated: June 3, 2019)

The first dedicated search for ultra-high energy (UHE) tau neutrinos of astrophysical origin was performed using the IceCube detector in its 22-string configuration. The search also had sensitivity to UHE electron and muon neutrinos. After application of all selection criteria to approximately 200 live-days of data, we expect a background of 0.60 ± 0.19 (stat.) $^{+0.56}_{-0.58}$ (sys.) events and observe three events, which after inspection emerge as being compatible with background. Therefore, we set an upper limit on neutrinos of all flavors from UHE astrophysical sources at 90% CL of $E^2\Phi(\nu_x) < 16.2 \times 10^{-8} \text{ GeV cm}^{-2} \text{ sr}^{-1} \text{ s}^{-1}$ over an estimated primary neutrino energy range of 340 TeV to 200 PeV.

PACS numbers: 95.85.Ry, 14.60.Lm, 95.30.Cq, 95.55.Vj, 14.60.Fg
Keywords: IceCube, neutrino telescope, tau neutrinos, double bangs

I. INTRODUCTION

Proposed astrophysical sources of observed ultra-high energy (UHE) cosmic rays are expected to also produce ultra-high energy neutrinos, mainly via charged pion decay following interactions on ambient matter and radiation [1, 2]. Candidate neutrino sources include active galactic nuclei, gamma ray bursts and microquasars [3–5]. Neutrinos are expected to arrive at Earth with a flavor ratio of $\nu_e:\nu_\mu:\nu_\tau = 1:1:1$ in the standard neutrino oscilla-

tion scenario [7]. Other neutrino production and propagation models predict different flux ratios at Earth [8–10]. If there are many astrophysical point sources of neutrinos, but each one is too weak to be distinguished individually from background, then a suitable detection strategy is to perform a cumulative search for “diffuse” flux of UHE neutrinos over the full available solid angle.

In previous searches [11–13], diffuse astrophysical UHE neutrinos were distinguished from atmospheric neutrinos by requiring the energy of candidate UHE neutrino events to exceed a certain threshold. In this work, we present techniques for identifying ν_τ interactions and show the results of the first search for diffuse astrophysical UHE neutrinos that specifically selected events consistent with several ν_τ interaction topologies.

At $E_\nu \gtrsim 1 \text{ PeV}$, a search for UHE ν_τ offers several advantages over UHE ν_e and ν_μ searches. Partially and fully contained interactions of UHE ν_τ in the detector can

* Physics Department, South Dakota School of Mines and Technology, Rapid City, SD 57701, USA

† Los Alamos National Laboratory, Los Alamos, NM 87545, USA

‡ also Sezione INFN, Dipartimento di Fisica, I-70126, Bari, Italy

§ Corresponding author: Seon-Hee Seo. seo@fysik.su.se

¶ NASA Goddard Space Flight Center, Greenbelt, MD 20771, USA

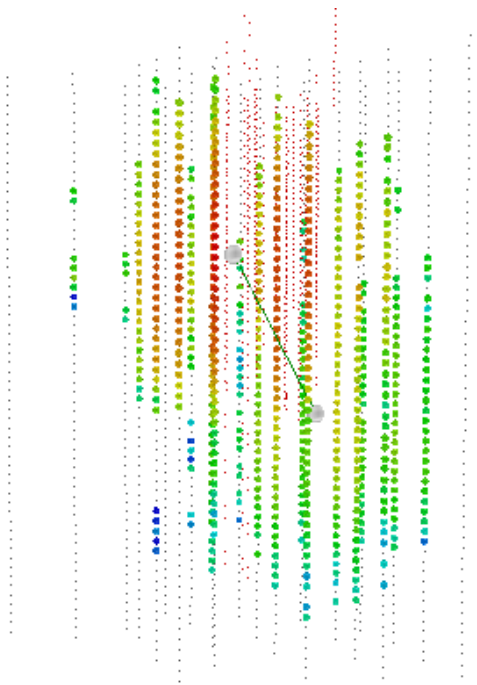


FIG. 1. A simulated double bang event with a primary ν_τ energy of 47 PeV entering the IC22 detector at a zenith angle of 35° . The two bigger circles in gray color represent the vertexes of tau creation (upper left) and decay (lower right) which are connected by a tau track. Each smaller circle represents a photomultiplier tube (PMT) that observed light produced by the event. The arrival times are indicated by colors that are ordered following the colors of the rainbow, with red corresponding to earlier times and violet to later times.

produce very distinctive signatures owing to the macroscopic τ decay length. Each such signature should appear in proportion to the well-measured τ branching ratios [14], providing a useful cross-check on the positive identification of multiple ν_τ events. As shown below, the chief sources of possible background events are unlikely to mimic these signatures. Also, at these energies there is negligible intrinsic ν_τ background in the conventional atmospheric neutrino flux [15]. The prompt ν_τ flux from charm hadron decays in cosmic-ray-induced air showers is also expected to be small [16–18]. The signal ν_τ are expected to come from the vicinity of the horizon since there is insufficient material for interactions in the downward-going direction and ν_τ passing through the Earth emerge [19] at energies too low to create a UHE signature.

The ν_τ event topology depends on how much of the event is contained in the detector, the ν_τ energy, and the composition of the τ decay products. In this work only non-muonic τ decays were considered. A partially contained UHE ν_τ having only the decay vertex of τ in the fiducial volume is denoted a “lollipop,” while one having only the production vertex of the τ in the fiducial volume is denoted an “inverted lollipop.” A fully

contained UHE ν_τ having both production and decay vertices well separated in the fiducial volume is denoted a “double bang” [20]. Fig. 1 shows a simulated double bang event in the 22-string configuration of the IceCube detector (IC22).

Applying criteria to identify lollipop, inverted lollipop and double bang signatures produced by ν_τ interactions, we derived limits on the diffuse UHE ν_τ neutrino flux. We assumed a flux ratio of $\nu_e:\nu_\mu:\nu_\tau = 1:1:1$ for this analysis. We used 282.4 live-days of data collected in 2007–2008 by IC22. We describe the IC22 detector in Section II and the experimental and simulated data samples in Section III. We present our analysis in Section IV and the results in Section V. We discuss systematic errors in Section VI and our conclusions in Section VII.

II. THE ICECUBE 22-STRING DETECTOR

The 22-string configuration of IceCube (IC22) was deployed in early 2007, began taking physics-quality data in May of that year, and ended at the transition to IceCube’s 40-string configuration in April 2008. Each string consists of 60 digital optical modules (DOMs) buried deep in the icecap at the South Pole, with regular 17 m vertical spacing from 1450 to 2450 m below the surface, for a total of 1320 DOMs. The strings are situated on a regular grid with 125 m horizontal interstring spacing, covering the area shown in Fig. 2. Each DOM houses

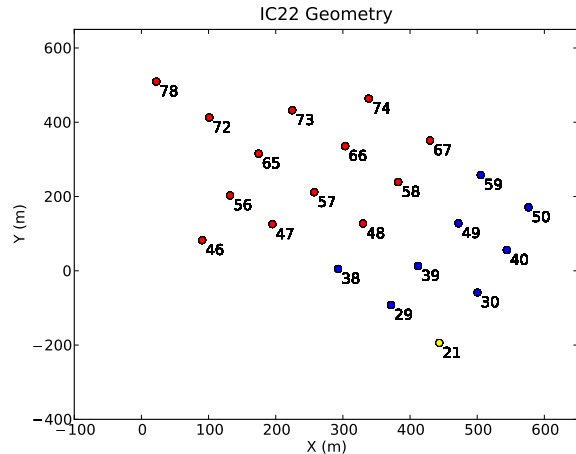


FIG. 2. Top view of the IceCube 22 string detector. Each string is represented as a dot with its associated string number.

a photomultiplier tube (PMT) to detect the Cherenkov light, electronics for pulse digitization and other functions, and remotely-controllable calibration light sources. To reduce the impact of PMT signals due to random noise, only detected signals with minimum 0.25 single photoelectron (pe) PMT pulse height were digitized by two types of waveform digitizers *in situ*: the ATWD

(Analog Transient Waveform Digitizer) and an fADC (Fast Analog to Digital Converter). The time resolution of the ATWD (fADC) is about 3.33 ns (25 ns) with a readout time window of about 450 ns ($6.4 \mu\text{s}$). Thus the ATWD is used to capture detailed waveform information on a short time scale while the fADC records less detailed information on a longer time scale. The ATWD also supports three channels with different gains ($\times 16$, $\times 2$, and $\times 0.25$) to extend its effective dynamic range.

To further remove random noise the digitized signal in a DOM was required to be in close temporal coincidence with a signal in neighboring DOMs. The signals satisfying such a temporal condition in hardware are called LC (Local Coincidence) hits. LC hits were then checked to see whether or not they satisfied a software-based trigger that selected for patterns potentially produced by a charged particle. Groups of hits that satisfied a trigger condition were packaged into “events.” Higher-level “filter” algorithms were applied to each event, and those events passing one or more filter conditions were transmitted over satellite to the northern hemisphere for higher-level analysis. However, all the data satisfying the software trigger conditions were stored on tape and shipped to the northern hemisphere. The software trigger and filter conditions applied to the data used in this analysis are described in the section below. For more detail on the design, construction and performance of IceCube in general, see [21–24] and references therein.

III. DATA

A. Experimental Data

The DOM signals satisfying the LC condition were required by the online data acquisition (DAQ) system at the surface computing system in the IceCube Laboratory to satisfy a “simple majority trigger” condition under which eight or more DOMs reported signals in a $5 \mu\text{s}$ time window (“SMT8”). The IC22 trigger rate of 500 to 620 Hz followed the seasonal variation in the cosmic-ray muon flux. The DAQ system grouped together DOM hits satisfying the trigger condition into an event using a broadened $\pm 8 \mu\text{s}$ time window. Triggered events used in this analysis were accepted if they also satisfied the extremely high energy (EHE) filter applied to the data online at the South Pole to reduce low energy events consistent with background. The EHE filter required ≥ 80 DOMs registering hits in the event.

We split off about 30% of the full IC22 dataset (82.4 live-days, uniformly distributed in time across the data-taking period) to use in conjunction with simulated data in the design of our subsequent selection criteria. In keeping with our procedures for maintaining blindness in the analysis of data, and thereby reducing human bias in the analysis of the data, the final result is based on the application of these selection criteria, unaltered, to the remaining 70% of the dataset (200 live-days).

B. Simulated Data

We employed simulated data to develop criteria that enhanced a possible astrophysical neutrino signal while diminishing backgrounds from atmospheric neutrinos and cosmic-ray muons. Exclusive use of simulated data also permitted us to maintain blindness. For the signal, the ANIS (All Neutrino Interaction Simulation) package [25] was used to produce each neutrino flavor separately. They were generated following an E^{-1} energy spectrum to enhance event statistics at higher energy where this analysis is sensitive. The events were then run through the IceCube detector simulation. The muon (electron) neutrinos were generated over all zenith angles in the energy range between 10(50) GeV to 10 EeV while tau neutrinos were generated between 1 TeV and 1 EeV.

Cosmic-ray muon backgrounds were simulated by generating air shower events using the CORSIKA package [26], then propagating the muons to and through the detector volume with the MMC package [27], and finally applying the detector simulation to the resulting set of particles.

For solitary air showers, a two-component model [28] was used. In this model, the entire mass spectrum of cosmic rays is approximated by only proton and iron components. Compared to Hörandel’s polygonato model [29], the two-component model agrees better with experimental data at higher energy (beyond 100 TeV) where this analysis is sensitive. The cosmic ray primaries are sampled with an E^{-2} spectrum. In this way we were able to produce events more efficiently at the higher primary energies that contribute most strongly to the background at ultra-high energies. The cosmic ray flux was then re-weighted to match the expected spectrum.

The acceptance of IC22 admits the possibility of detecting muons from multiple quasi-simultaneous air shower events, so we also simulated muons from two coincident air shower events. (Higher multiplicities occur at a negligible rate in IC22 and were not simulated.) For coincident air showers, Hörandel’s polygonato model of cosmic rays was used. Solitary(coincident) atmospheric air showers were generated with energies between 10(0.6) TeV–100 EeV and zenith angles between 0 – 90° .

After event generation and detector simulation, the simulated data were processed in the same way as real data, i.e., with sequential applications of trigger and filter conditions, as described earlier.

IV. TAU NEUTRINO IDENTIFICATION

A. Selection Criteria

Based on the characteristics of simulated data, we formulated several event selection criteria to exploit the UHE ν_τ signatures of a track plus one or two showers, in

contrast to conventional pure track-like or pure shower-like events. Two such criteria use the reconstructed number of photoelectrons (N_{pe}) per DOM as a function of time, denoted $N_{pe}^{DOM}(t)$. Fig. 3 shows $N_{pe}^{DOM}(t)$ for a simulated inverted lollipop (top) and a simulated muon event (bottom). Note that the times of the hits are with respect to the event trigger time which has an extended readout time window of $\pm 8 \mu s$ in IC22. For this reason, all the hit times exhibit at least a $\pm 8 \mu s$ offset.

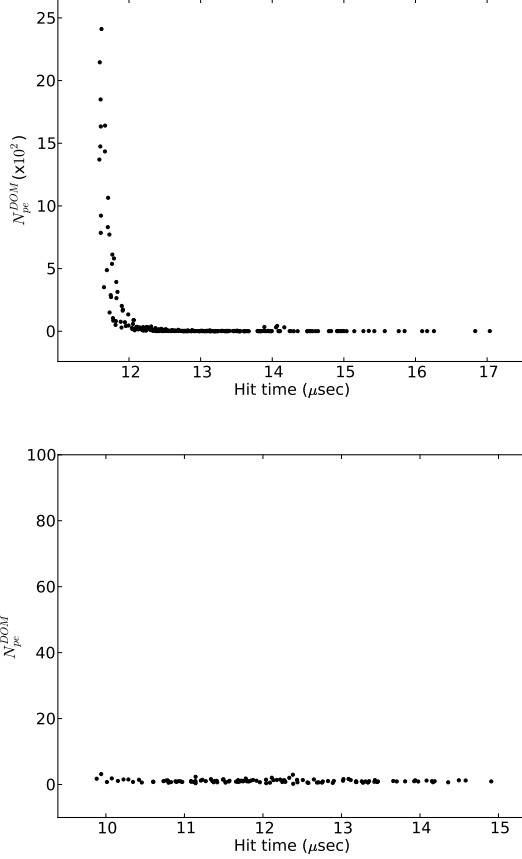


FIG. 3. The quantity $N_{pe}^{DOM}(t)$ for a simulated inverted lollipop (top) and a simulated muon event (bottom), with primary particle energies of 25.4 PeV and 2.38 PeV, respectively.

To exploit the power of $N_{pe}^{DOM}(t)$, we devised a parameter called “maximum current ratio” (IR_{max}), defined as the maximum of I_{in}/I_{out} where $I_{in(out)} = \Delta Q_{in(out)}/\Delta T_{in(out)}$. Here, ΔQ_{in} was the charge, measured in photoelectrons, collected by the DOMs in a sliding time window of length ΔT_{in} . The time window was optimized in this analysis to be $1.2 \mu s$ long. The corresponding “out” variables were the charge and time measured outside the sliding time window (see Fig. 4). As shown in Fig. 5, IR_{max} is small for track-like events and large for events containing showers, such as those produced by ν_τ . Since the IR_{max} cut is related to energy, it will be applied to data as the last cut together with

the other energy related cut explained at the end of this sub-section.

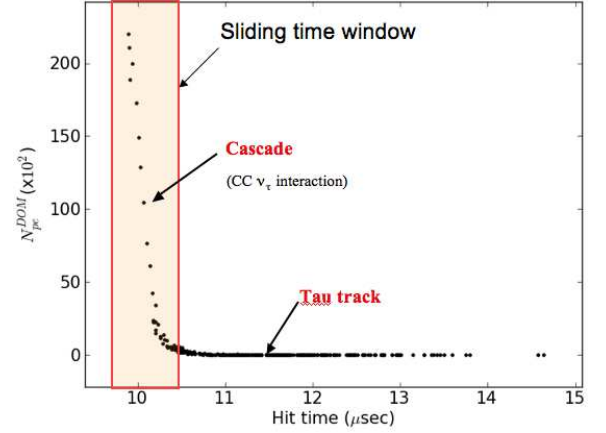


FIG. 4. Illustration of the IR_{max} parameter. See text for the explanation.

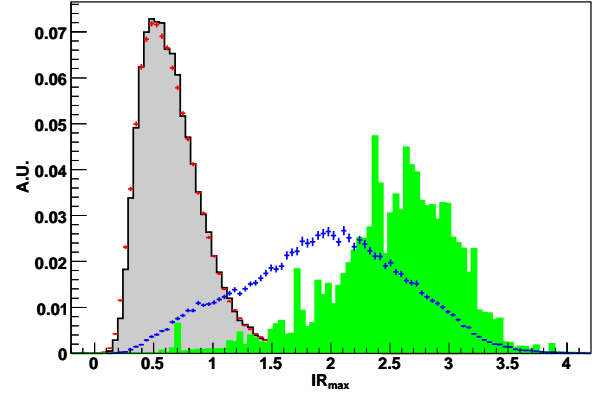


FIG. 5. The parameter IR_{max} for simulated signal (green histogram for lollipop and blue points for all ν_τ events) and background (red points for atmospheric muon) events, and for data (gray histogram) passing the EHE filter. The separation of signal from background is evident. The IR_{max} distributions of inverted-lollipop and double bang events are also well-separated from the background.

Although IR_{max} is very effective at distinguishing most simple track-like background events from signal events, highly energetic muons can stochastically deposit large amounts of energy along their track lengths via Bremsstrahlung, pair production, or photonuclear interactions, potentially mimicking ν_τ events. Fig. 6 shows an example of simulated muon with such a Bremsstrahlung whose IR_{max} value could be similar to that of a ν_τ . Theoretically, ν_τ events are most likely to have a large $N_{pe}^{DOM}(t)$ at one or both of the temporal edges of the event. In practice, ν_τ events had a large $N_{pe}^{DOM}(t)$ in

the earliest third due to the presence of highly scattered photons that extended the temporal edge of the event to much later times. We expect future analyses to be able to devise criteria that reduce the impact of these scattered photons. The “local charge density” (ρ_q) parameter was introduced to remove events consistent with a large energy deposit away from either temporal edge.

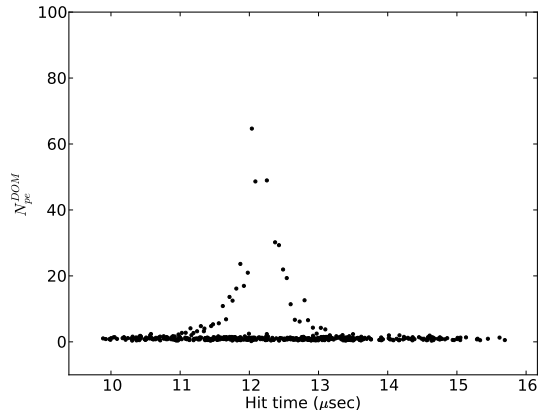


FIG. 6. The quantity $N_{pe}^{DOM}(t)$ for a simulated muon event (336 PeV) with an energetic Bremsstrahlung.

Dividing each event into equal thirds in time, ρ_q was defined in each third as the total charge-to-time ratio. The event was rejected when $\rho_q < 5 N_{pe} / ns$ in either the first or last third. Figure 7 illustrates the ρ_q parameter and shows how it can distinguish ν_τ events from muon Bremsstrahlung events. Figure 8 quantifies the ability of ρ_q to separate signal from background.

Additional selection criteria were applied to further remove backgrounds. The flux of downward-going muons from cosmic-ray air shower events was reduced by implementing a “veto layer” in software, removing any events in which the average Z position of the first 4 hits (\bar{Z}_{init}), was in the top 50 m of the detection volume. Downward-going muons were further removed using the approximate event velocity \bar{V}_Z (m/ns), constructed from the difference between the positions Z_{cog} and \bar{Z}_{init} , divided by the difference in their respective times, *i.e.*, T_{cog} and \bar{T}_{init} , where Z_{cog} (T_{cog}) were the Z position (time) of the center of gravity of all hit DOMs. The times here are calculated using the average time of the hits used to calculate the Z positions. We removed events consistent with a downward direction by requiring $\bar{V}_Z < -0.1$ m/ns.

Background events arising from muon stochastic processes at or near the bottom of the detector, events whose muon tracks may go undetected, are removed by restricting our sample to events that were reasonably well-contained in the detector fiducial volume. We required the average depth position of all DOMs with signals to satisfy $Z_{cog} > -330$ m (as measured from the center of the detector).

We also applied a generic topological selection by cal-

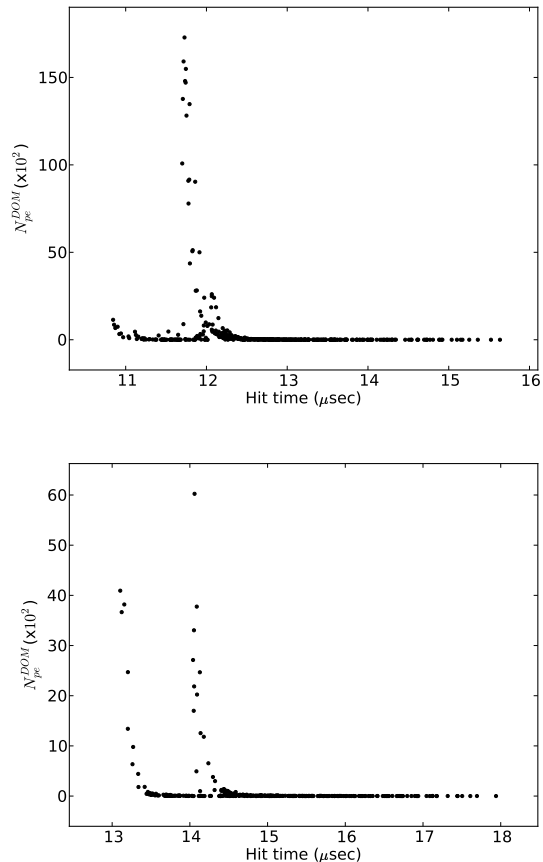


FIG. 7. The quantity $N_{pe}^{DOM}(t)$ for a simulated lollipop (top) and double bang (bottom) event. $N_{pe}^{DOM}(t)$ is shown for a simulated inverted lollipop in Fig. 3 (top) for an atmospheric muon event in Fig. 6. The atmospheric muon, with a Bremsstrahlung roughly in the middle of its contained track length, would be rejected by the cut on ρ_q described in the text, whereas the lollipop, inverted lollipop and double bang would not because the bulk of the detected light occurs sufficiently early in the event.

culating the eigenvalues of the tensor of inertia (ToI) of pulse amplitudes (instead of conventional mass) [30] from hit DOMs of each event and keeping only those events that tended towards sphericity. Perfectly spherical events will have three equal ToI eigenvalues, while perfectly track-like events will have one eigenvalue equal to zero. We therefore required that the ratio of smallest eigenvalue to the sum of all three eigenvalues was > 0.1 .

Remaining lower energy events were further reduced in number by requiring a minimum N_{pe} for each event. We required both $IR_{max} \geq 200$ and $\log_{10} N_{pe} \geq 4.2$, the values of which were based on an optimization that is described in the following section. Figure 9 shows the distributions of these two selection criteria for simulated signal, simulated background, and 30% of the data, prior to the overall optimization of all the selection criteria.

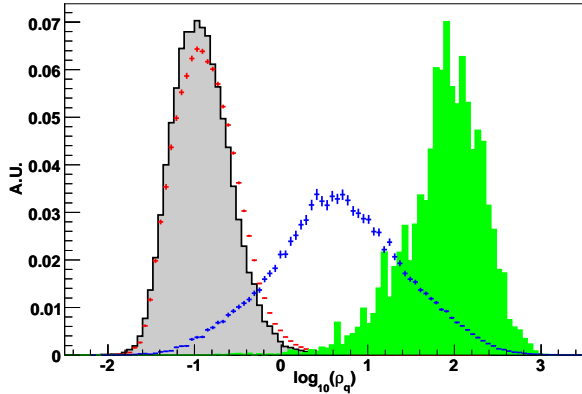


FIG. 8. The logarithm of the local charge density parameter (ρ_q) for signal (green histogram for lollipop and blue points for all ν_τ events) and background (red histogram for atmospheric muon) events, and for data (gray histogram) passing the EHE filter. The separation of signal from background is evident. The ρ_q distributions of inverted-lollipop and double bang events are also well-separated from the background.

B. Optimization of Selection Criteria

The final values for IR_{max} and N_{pe} were optimized by minimizing the Model Rejection Factor (MRF) [31] before applying them to the full dataset. We varied the values of IR_{max} and $\log_{10} N_{\text{pe}}$ as shown in Fig. 10, finding a shallow minimum at $\text{MRF} \sim 0.89$. At this MRF, the expected all-flavor signal and background were 3.52 and 0.81 events, respectively, using the Waxman-Bahcall upper bound [4] for the signal neutrino flux normalization with E^{-2} spectrum. The corresponding optimized values are $\text{IR}_{\text{max}} \geq 300$ and $\log_{10} N_{\text{pe}} \geq 4.0$. However, in order to be conservative in the face of limited simulated event statistics, we chose instead to use $\text{IR}_{\text{max}} \geq 200$ and $\log_{10} N_{\text{pe}} \geq 4.2$, resulting in an $\text{MRF} = 0.93$ and expected all flavor signal and background event counts of 3.18 and 0.60, respectively.

C. Selection efficiency

The event rates for the selection criteria described in Section IV A were grouped into sets (EHE, S1-4) for reference purposes and are summarized in Table I for simulated signals and Table II for simulated background and 30% of the data sample. It is evident from Table I that this analysis, though designed to be sensitive primarily to UHE ν_τ signals, also had appreciable sensitivity to UHE ν_e and ν_μ signals. The final limit described below will therefore be applicable to all neutrino flavors. Figures 11-14 show the distribution of event rates (Hz) for each cut parameter for simulated signal and background, and a sample of IC22 data after application of the EHE

filter (Fig. 11) and sets of selection criteria S1 (Fig. 12), S2 (Fig. 13), and S3 (Fig. 14).

The event selection efficiency of the different cuts can be obtained from Fig. 15 (top), where the simulated background and 30% of the data sample match well at each cut level. Figure 15 (bottom) shows the effective area A_{eff} for each neutrino flavor after application of the SMT8 trigger condition and the full suite of selection criteria. Using simulated signal, A_{eff} is defined by $\Phi_\nu A_{\text{eff}} T = N_{\text{det}}$, where Φ_ν is the neutrino flux prior to any propagation or interaction effects in the Earth, T is a length of time, and N_{det} is the number of detected events.

Figure 16 shows the distribution of the true zenith angle from the simulation as a function of the primary ν_τ energy for the events that passed all the selection criteria. As expected, most ν_τ were from near the horizon, with the angular acceptance peaking at about 100° from vertical.

V. RESULTS

After unblinding the remaining 200 live-days of data and applying all the selection criteria, three events remained in the data sample. The predicted background from all simulated sources was 0.60 ± 0.19 events. The remaining data events are shown in Fig. 17.

From a detailed study of these events, we determined that one was consistent with light produced by an AMANDA optical module observed to emit light intermittently (Fig. 17, top). A second event was qualitatively consistent with background from a nearly horizontal muon interacting near the bottom of the detector (Fig. 17, middle). The third event had the characteristics of a neutrino-induced shower (Fig. 17, bottom), and was also in the final sample of an independent IC22 analysis that searched for shower-like signals [33]. However, we can not rule out this event as being produced by a cosmic-ray muon accompanied by a stochastic high-energy Bremsstrahlung. We have conservatively treated all three events as background in the derivation of the final result.

VI. SYSTEMATIC AND STATISTICAL ERRORS

The systematic and statistical errors in this analysis were obtained using signal and background simulations and are summarized in Table III. In the following subsections, systematic errors on signal and background are explained followed by our result including both errors.

A. Systematic Errors for Signal

The systematic error due to our lack of precise knowledge of the DOM sensitivity to photons was obtained by simulating the effect of setting it to 90% and 110% of its

TABLE I. Predicted signal event rates with statistical error after application of each set of selection criteria. LP, ILP and DB represent lollipop, inverted-lollipop and double-bang, respectively. For signal rates, the flux was normalized to the WB bound. (The first column provides labels for reference purposes in subsequent tables and figures.)

Set No.	Selection Criteria	MC simulation					
		Signal ν (E^{-2})					
		LP $\times 10^{-9}$ [Hz]	ILP $\times 10^{-9}$ [Hz]	DB $\times 10^{-9}$ [Hz]	ν_τ $\times 10^{-8}$ [Hz]	ν_μ $\times 10^{-8}$ [Hz]	ν_e $\times 10^{-8}$ [Hz]
EHE	NDOM > 80	3.48 ± 0.11	3.54 ± 0.09	4.45 ± 0.16	50.5 ± 0.5	119 ± 2.2	39.9 ± 0.7
S1	$\rho_q > 5 N_{\text{pe}}/\text{ns}$	3.42 ± 0.11	3.05 ± 0.08	4.30 ± 0.16	24.0 ± 0.3	29.3 ± 0.8	23.9 ± 0.6
S2	$\bar{Z}_{\text{init}} < 450$ m, $\bar{V}_Z < -0.1$ m/ns	2.55 ± 0.10	2.91 ± 0.08	3.95 ± 0.16	22.6 ± 0.3	24.9 ± 0.8	22.9 ± 0.5
S3	$Z_{\text{cog}} > 330$ m, ToI > 0.1	2.32 ± 0.10	2.29 ± 0.08	3.02 ± 0.14	15.7 ± 0.3	11.8 ± 0.6	17.5 ± 0.5
S4	$\text{IR}_{\text{max}} \geq 200$, $\log_{10} N_{\text{pe}} \geq 4.2$	1.72 ± 0.08	1.72 ± 0.06	2.07 ± 0.11	5.63 ± 0.08	3.70 ± 0.15	9.08 ± 0.2

TABLE II. Predicted background event rates with statistical error after application of each set of selection criteria. For conventional neutrinos (labeled “conv” in the table), the Bartol model [15] was used. For prompt neutrinos, the Martin GBW model [32] was used for ν_τ and the Sarcevic standard model [17] was used for ν_μ and ν_e .

Set No.	MC simulation						Data
	Background ν					Background μ	30 % sample
	ν_{μ}^{conv}	ν_e^{conv}	$\nu_{\tau}^{\text{prompt}}$	$\nu_{\mu}^{\text{prompt}}$	ν_e^{prompt}		
	$\times 10^{-8}$ [Hz]	$\times 10^{-8}$ [Hz]	$\times 10^{-10}$ [Hz]	$\times 10^{-8}$ [Hz]	$\times 10^{-8}$ [Hz]		
EHE	184 ± 14.0	6.88 ± 0.26	33.4 ± 0.4	23.6 ± 0.50	9.95 ± 0.13	830,000	$1,370,000 \pm 438$
S1	8.21 ± 1.80	0.96 ± 0.06	9.74 ± 0.17	2.19 ± 0.12	3.46 ± 0.05	303	246 ± 5.9
S2	8.11 ± 1.80	0.96 ± 0.06	9.62 ± 0.17	2.05 ± 0.12	3.42 ± 0.05	41.2	53.3 ± 2.7
S3	4.16 ± 0.66	0.70 ± 0.06	7.12 ± 0.14	1.26 ± 0.09	2.55 ± 0.04	14.4	20.8 ± 1.7
S4	0.24 ± 0.06	0.04 ± 0.003	0.91 ± 0.03	0.15 ± 0.02	0.43 ± 0.01	0.026 ± 0.01	0

nominal value resulting in $[-4.7\%, +7.9\%]$ error. The systematic error in the event rates reflecting uncertainties on the optical properties of the ice was obtained by simulating events using different ice models. The ice models were created from data generated using *in situ* light sources. The baseline ice model [34] for this analysis used optical properties of the ice measured at AMANDA depths and extrapolated to IceCube depths, while an alternative ice model [35] obtained them with a direct fit to the full range of IceCube light source data. Comparing the predictions of the two ice models resulted in a +29.4% error.

The systematic uncertainty in the neutrino cross section came from two sources. One was from theoretical uncertainty in the parton distribution function evaluation and structure function and the other was from errors in the experimental measurement of the parton distribution function by HERA [36]. From these two sources we estimated the systematic error in the neutrino cross section as $\pm 6.4\%$. Very high energy events could saturate PMTs by exceeding the PMT’s dynamic range. This could result in an incorrect estimation of the original neutrino energy. Since the observable quantity most closely related to the energy is N_{pe} , the systematic error associated with the PMT saturation was obtained by observing the impact of changing the N_{pe} cut from 90% to 110% of its original value. This error was found to be $[-5.7\%, +5.0\%]$.

B. Systematic Errors for Background

The systematic errors due to uncertainties in DOM sensitivity, ice properties, and DOM saturation behavior were obtained in the same manner as for the signals, as described in Section VI A. They were estimated as $[-4.7\%, +7.9\%]$, $[-62\%, +85\%]$, and $[-28.9\%, +5.3\%]$, respectively.

In addition, there are systematic errors which applied only to the background. The muon event rate is known to change as a function of the atmospheric temperature above the South Pole plateau. Since our muon simulation assumed a rate pegged to that seen in October, the seasonal variation was taken into account as a systematic error and was estimated as $[-24\%, +18\%]$ when compared with IC22 data at EHE filter level. The systematic error due to cosmic ray composition was also obtained by switching constants and slopes between proton and iron in the two component model data. At S3, just before the final cut to have enough statistics, we obtained -24% by this method.

There are alternative models for the prompt neutrino flux. For this analysis, the base models used for the prompt neutrino flux are Sarcevic standard flux model for ν_μ and ν_e [17], and Martin GBW model for ν_τ [32]. As an alternative, we have also considered the Sarcevic minimum and maximum flux models [17], from which we

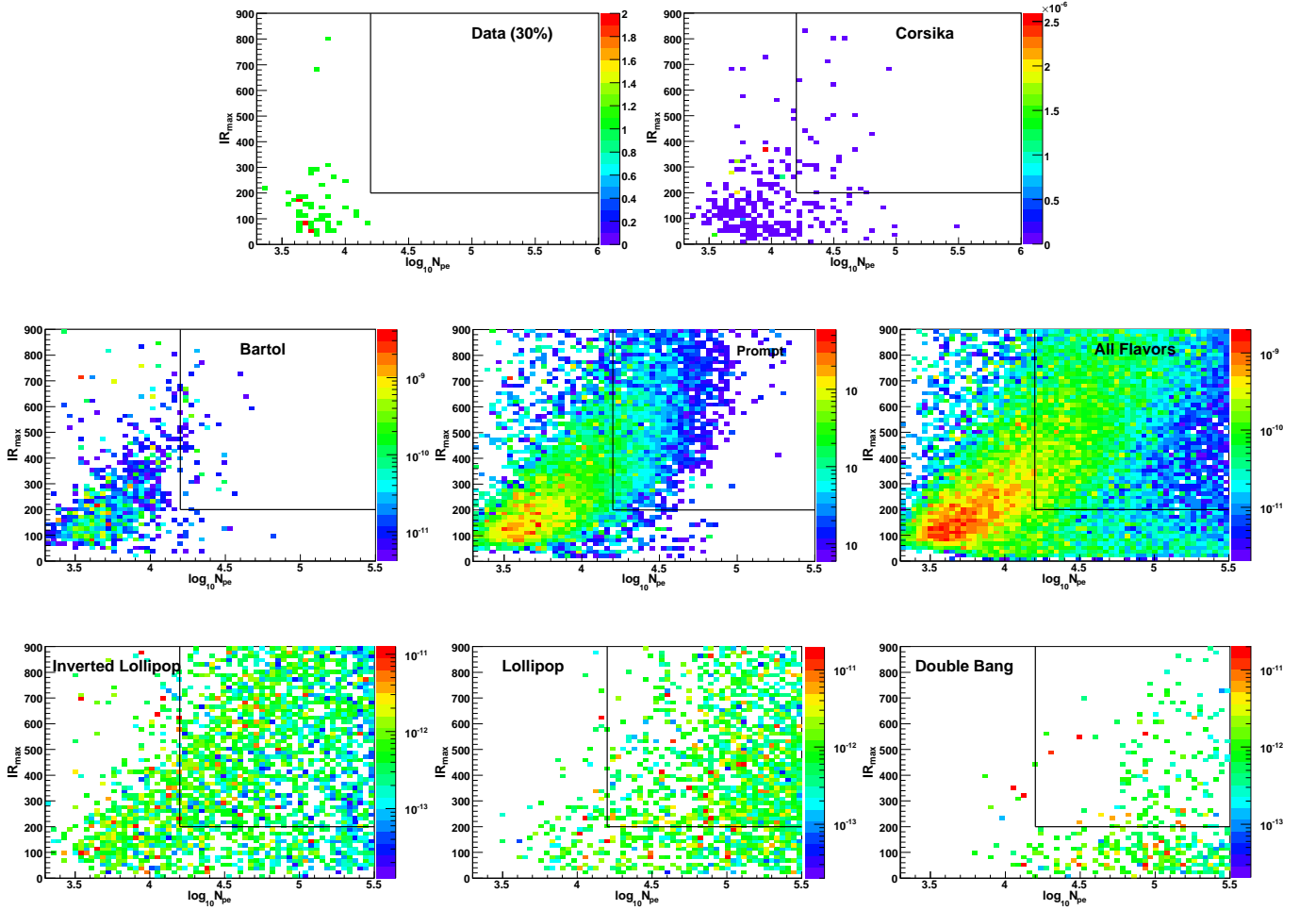


FIG. 9. Distributions of the quantities IR_{\max} vs. $\log_{10} N_{pe}$ for 30% of the data (row 1, left), simulated cosmic-ray background (row 1, right), simulated atmospheric neutrinos (row 2, left), simulated prompt atmospheric neutrinos (row 2, middle), simulated all-flavor neutrino signal (row 2, right), and ν_τ inverted lollipop (row 3, left), lollipop (row 3, middle) and double bang (row 3, right), assuming an E^{-2} spectrum and prior to selection criteria optimization. The color code represents the event rate in Hz except for the data where it represents number of events in 30% of the data sample (82.4 live-days). The region in the upper right of each plot, indicated by the black lines, designates the region selected by the optimized criteria as described in Section IV B.

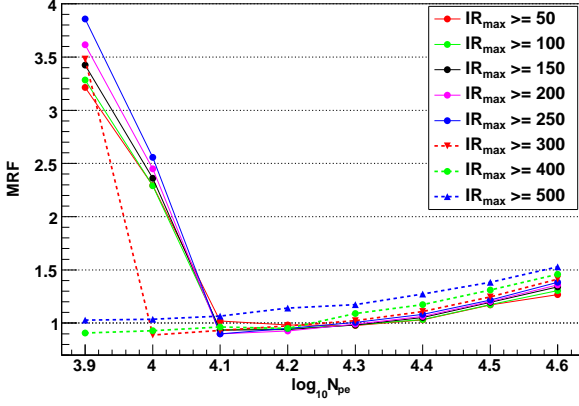


FIG. 10. We tuned the selection criteria IR_{\max} and $\log_{10} N_{pe}$ using the Model Rejection Factor (MRF) formalism. The plot shows how the MRF varies as a function of $\log_{10} N_{pe}$ for different values of IR_{\max} . We chose values for these parameters near but not exactly at the minimum shown for reasons explained in the text.

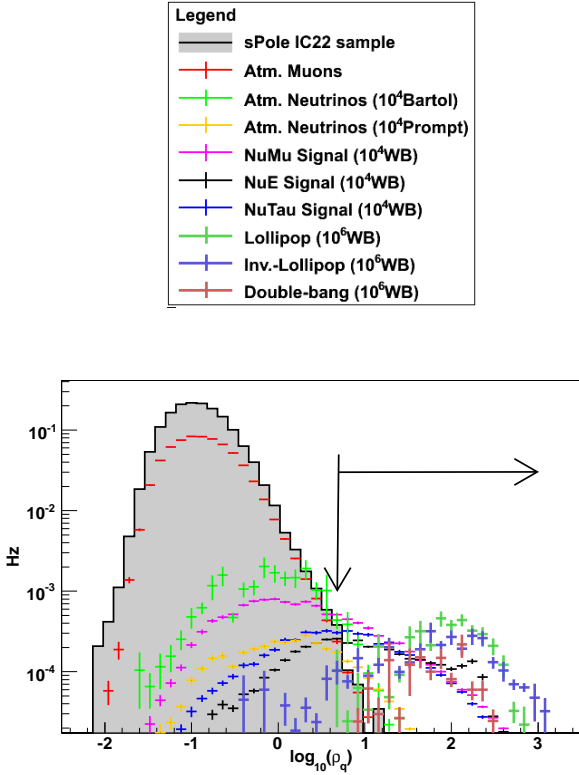


FIG. 11. Distributions of selection criteria for signal, BG, and 30% of the IC22 data just before application of the “S1” set of selection criteria. The vertical (horizontal) arrow line represents the cut value (selected region) of that set.

estimate a $[-59\%, +30\%]$ systematic error on the prompt neutrino flux.

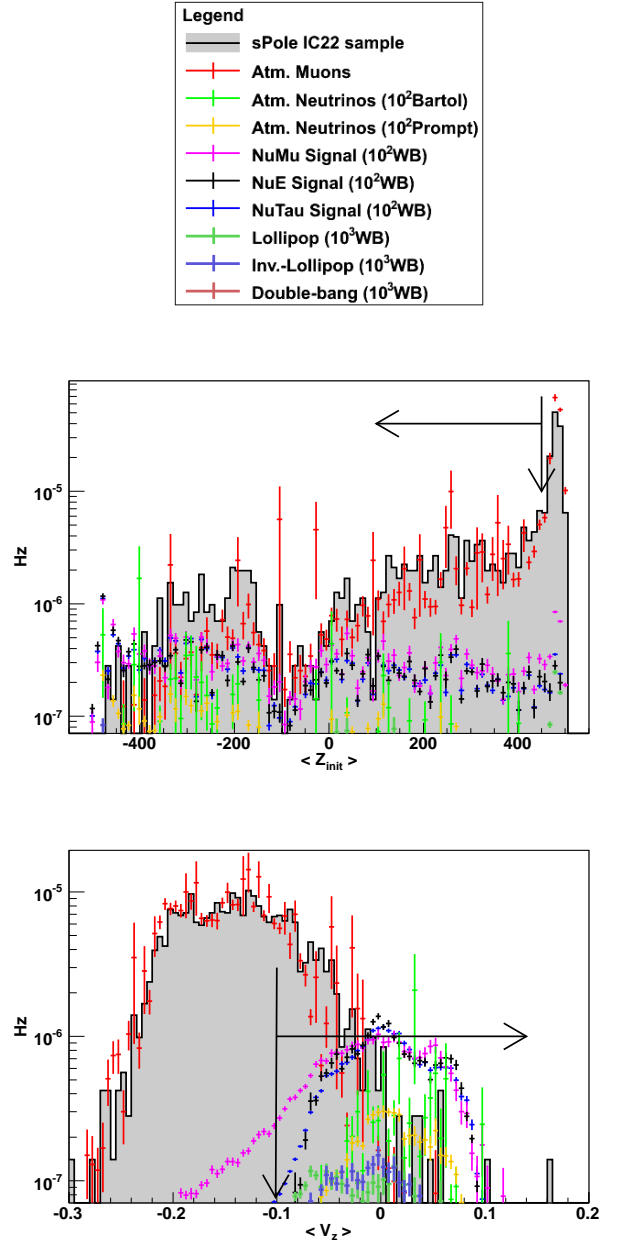


FIG. 12. Distributions of selection criteria for signal, BG, and 30% of the IC22 data just before application of the “S2” set of selection criteria. The vertical (horizontal) arrow lines represent the cut values (selected regions) of that set.

C. Result including Statistical and Systematic Errors

Since it was computationally feasible to generate a large amount of simulated signal, the statistical error on the simulated signal is small ($\pm 2.3\%$). By contrast, the considerably larger statistical error on the simulated background ($\pm 39\%$) reflects the aggregate effect of the high rejection efficiency of our selection criteria and the limitations imposed by finite computational resources.

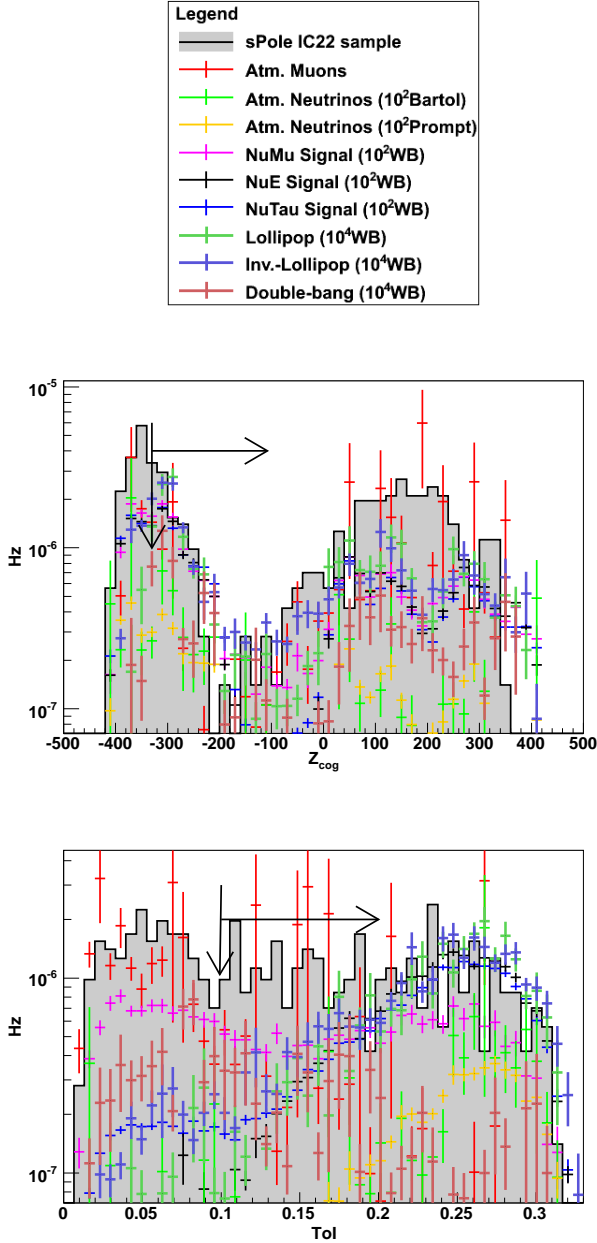


FIG. 13. Distributions of selection criteria for signal, BG, and 30% of the IC22 data just before application of the “S3” set of selection criteria. The vertical (horizontal) arrow lines represent the cut values (selected regions) of that set.

We combined the systematic and statistical errors and applied a profile log-likelihood method [37] to derive the following limit on the astrophysical all-flavor neutrino flux at 90% CL [38]: $E^2\Phi(\nu_x) < 16.2 \times 10^{-8} \text{ GeV cm}^{-2} \text{ sr}^{-1} \text{ s}^{-1}$ for the 3 observed events from the 200 live-days of IC22 data. This limit applies to the primary neutrino energy range of $340 \text{ TeV} < E_\nu < 200 \text{ PeV}$, covering the middle 90% of the accepted simulated signal. Fig. 18 shows this limits together with several theoretical model predictions. The upper limit

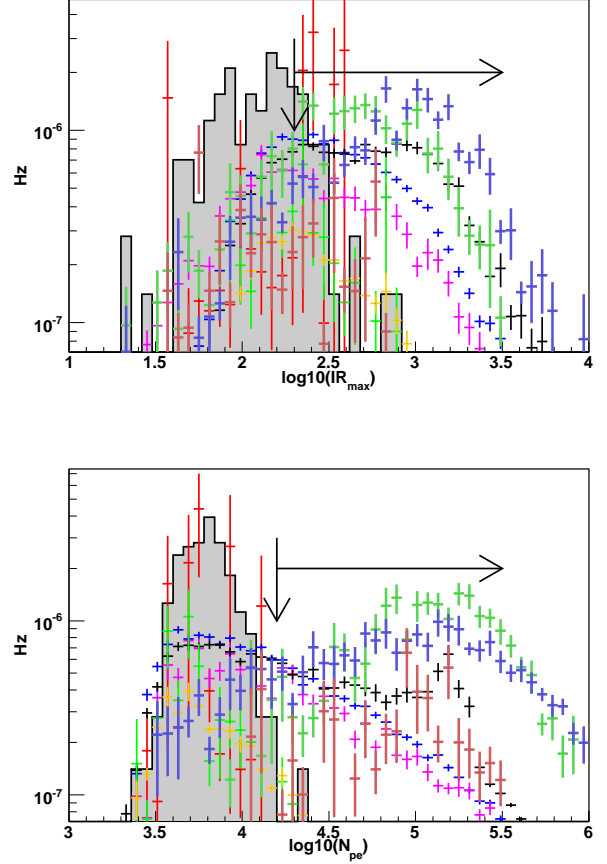


FIG. 14. Distributions of selection criteria for signal, BG, and 30% of the IC22 data just before application of the “S4” set of selection criteria. The vertical (horizontal) arrow lines represent the cut values (selected regions) of that set. The legend for these plots is the same as in Fig. 13.

on the tau neutrino flux is one third that of the all-flavor astrophysical neutrino flux if one assumes a flavor ratio of $\nu_e:\nu_\mu:\nu_\tau = 1:1:1$.

VII. CONCLUSIONS AND OUTLOOK

A set of selection criteria designed for UHE ν_τ detection were applied to IceCube data. These criteria also had appreciable efficiency for UHE ν_e and ν_μ detection. We applied these criteria to 200 live-days of data from IceCube’s 22-string configuration and observed 3 events compatible with background. We therefore set a 90% CL upper limit on the astrophysical UHE all-flavor neutrino flux of $E^2\Phi(\nu_x) < 16.2 \times 10^{-8} \text{ GeV cm}^{-2} \text{ sr}^{-1} \text{ s}^{-1}$. The analysis improves on the previous limit set by AMANDA [33, 39, 41] with comparable integrated exposure. Future IceCube searches specialized for ν_τ will be more sensitive due to the increased fiducial volume relative to IC22. The large vol-

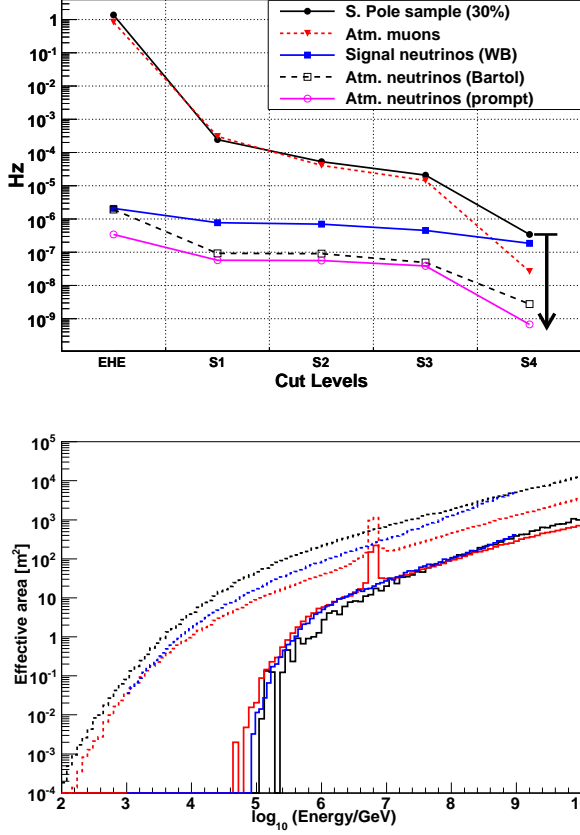


FIG. 15. Top: Event rate (Hz) at each cut level for simulated signal and background, and 30% of the data sample. At S4, there were zero events in the data sample, and so the 90% CL upper limit value was plotted as indicated by the black arrow. Bottom: IC22 effective areas for each neutrino flavor (black: ν_μ , red: ν_e , blue: ν_τ) after application of the SMT8 trigger (dashed lines) and after application of all selection criteria (solid lines).

ume will also warrant the application of sophisticated ν_τ reconstructions, further improving the sensitivity of these searches.

ACKNOWLEDGMENTS

We acknowledge the support from the following agencies: U.S. National Science Foundation-Office of Polar Programs, U.S. National Science Foundation-Physics Division, University of Wisconsin Alumni Research Foundation, the Grid Laboratory Of Wisconsin (GLOW) grid infrastructure at the University of Wisconsin - Madison, the Open Science Grid (OSG) grid infrastructure; U.S. Department of Energy, and National Energy Research Scientific Computing Center, the Louisiana Optical Network Initiative (LONI) grid computing resources; National Science and Engineering Research

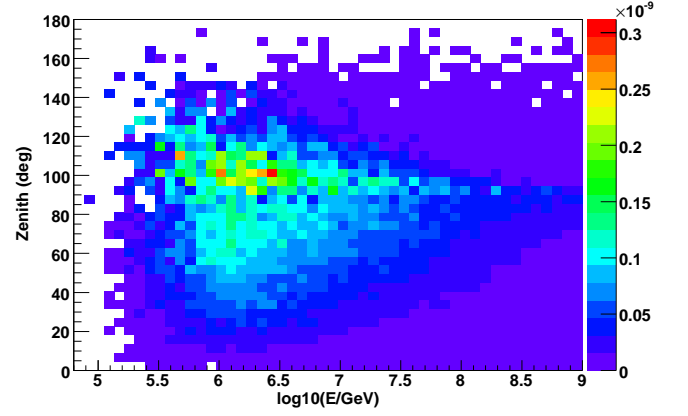


FIG. 16. The distribution of the true zenith angle from the simulation as a function of the primary ν_τ energy for the events passing all selection criteria. Color code represents event rate in Hz.

Council of Canada; Swedish Research Council, Swedish Polar Research Secretariat, Swedish National Infrastructure for Computing (SNIC), and Knut and Alice Wallenberg Foundation, Sweden; German Ministry for Education and Research (BMBF), Deutsche Forschungsgemeinschaft (DFG), Research Department of Plasmas with Complex Interactions (Bochum), Germany; Fund for Scientific Research (FNRS-FWO), FWO Odysseus programme, Flanders Institute to encourage scientific and technological research in industry (IWT), Belgian Federal Science Policy Office (Belspo); University of Oxford, United Kingdom; Marsden Fund, New Zealand; Australian Research Council; Japan Society for Promotion of Science (JSPS); the Swiss National Science Foundation (SNSF), Switzerland.

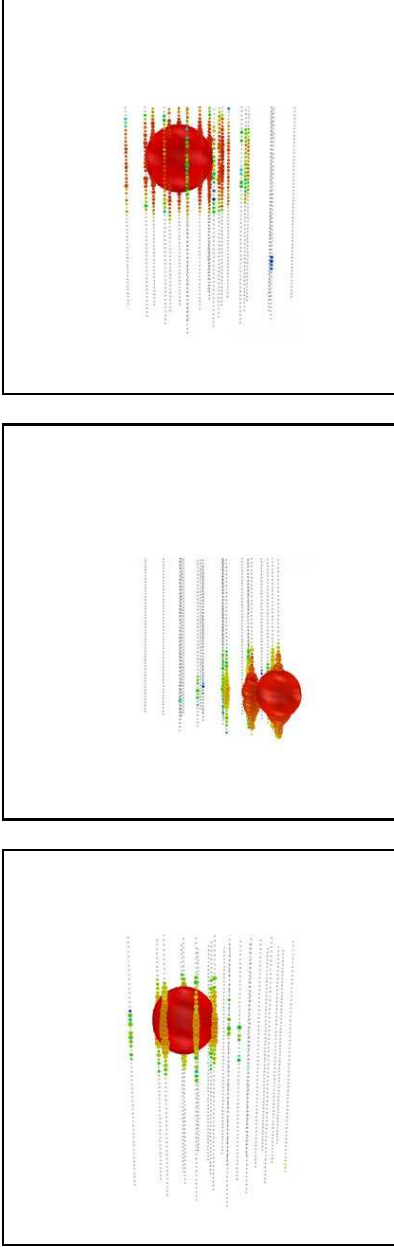


FIG. 17. Diagrams of the three events surviving the final selection criteria applied to the 200 live-days of IC22 data. The radius of each circle is proportional to the number of photons detected by the PMT.

TABLE III. Summary of the systematic and statistical errors for signal and background events from the simulated data.

Source	Signal	Background
DOM sensitivity	- 4.7%, + 7.9%	- 4.7%, + 7.9%
Ice properties	- 0%, + 29%	- 62%, + 85%
ν cross section	- 6.4%, + 6.4%	N/A
PMT saturation	- 5.7%, + 5.0%	- 29%, + 5.3%
Cosmic ray flux	N/A	- 0%, + 16%
Cosmic ray composition	N/A	- 24%, + 0%
Seasonal variation	N/A	- 24%, + 18%
Prompt ν flux model	N/A	- 59%, + 30%
Total syst. error	- 7.9%, + 31%	- 97%, + 94%

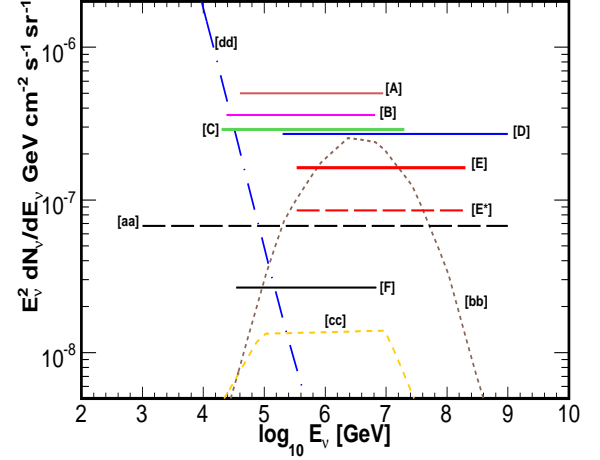


FIG. 18. The limits on production of UHE neutrinos. [A]: AMANDA-II cascade all flavor limit (1001 live-days) [39], [B]: IC22 cascade all flavor limit (257 live-days) [33], [C]: Baikal all flavor limit (1038 live-days) [40], [D]: AMANDA-II UHE all flavor limit (457 live-days) [41], [E]: IC22 UHE all flavor limit from diffuse sources using the analysis described in this paper (this work, 200 live-days), [E*]: IC22 UHE all flavor sensitivity (this work, 200 live-days), [F]: IC40 $\nu_\mu \times 3$ (375.5 live-days) [42], [aa]: Waxman Bahcall (ν_μ and $\bar{\nu}_\mu$) model $1998 \times \frac{3}{2}$ [4], [bb]: Stecker blazar model 2005 [43], [cc]: Waxman Bahcall Prompt GRB model [44], and [dd]: Atmospheric neutrino flux (Bartol + Sarcevic standard model)

-
- [1] F. Halzen and D. Hooper, Rept. Prog. Phys. **65**, 1025 (2002).
 - [2] J. Becker, Phys. Rept. **458**, 173 (2008).
 - [3] F.W. Stecker, C. Done, M.H. Salomon and P. Sommers, Phys. Rev. Lett. **66**, 2697 (1991).
 - [4] E. Waxman and J. Bahcall, Phys. Rev. Lett. **78**, 2292 (1997).
 - [5] A. Levinson and E. Waxman, Phys. Rev. Lett. **87**, 171101 (2001).
 - [6] L.A. Anchordoqui, D. Hooper, S. Sarkar and A.M. Taylor, Astropart. Phys. **29**, 1 (2008).
 - [7] J. G. Learned and S. Pakvasa, Astropart. Phys. **3**, 267 (1995).
 - [8] J. P. Rachen and P. Meszaros, Phys. Rev. **D58**, 123005 (1998).
 - [9] T. Kashti and E. Waxman, Phys. Rev. Lett. **95**, 181101 (2005).
 - [10] M. Kachelriess, S. Ostapchenko, and R. Tomas, Phys. Rev. **D77**, 023007 (2008).
 - [11] A. Achterberg et al., Phys. Rev. **D7**, 042008 (2007); M. Ackermann et al., Astrophys. J. **675**, 1014 (2008).
 - [12] J. Ahrens et al., Phys. Rev. **D67**, 12003 (2003); M. Ackermann et al., Astropart. Phys. **22**, 127 (2004).
 - [13] R. Abbasi et al., Astropart. Phys. **34**, 420 (2011).
 - [14] K. Nakamura *et al.* [Particle Data Group], J. Phys. G **37**, 075021 (2010).
 - [15] G.D. Barr, T.K. Gaisser, P. Lipari, S. Robbins, and T. Stanev, Phys. Rev. D **70**, 023006 (2004); G.D. Barr, T.K. Gaisser, S. Robbins, and T. Stanev, Phys. Rev. D **74**, 094009 (2006).
 - [16] G. Florentini, A. Naumov and F.L. Villante, Phys. Lett. **B510**, 173 (2001).
 - [17] R. Enberg, M.H. Reno and I. Sarcevic, Phys. Rev. **D78**, 043005 (2008).
 - [18] A.D. Martin, M.G. Ryskin and A.M. Stasto, Acta Polon. **B34** 3273 (2003).
 - [19] F. Halzen and D. Salzberg, Phys. Rev. Lett. **81**, 4305 (1998).
 - [20] J.G. Learned and S. Pakvasa, Astropart. Phys. **3**, 267 (1995).
 - [21] R. Abbasi et al., Nucl. Instrum. Meth. **A618**, 139 (2010).
 - [22] A. Achterberg et al., Astropart. Phys. **26**, 155 (2006).
 - [23] R. Abbasi et al., Nucl. Instrum. Meth. **A601**, 294 (2009).
 - [24] F. Halzen and S.R. Klein, Rev. Sci. Instrum. **81**, 081101 (2010).
 - [25] A. Gazizov and M. Kowalski, Computer Physics Communications **172**, 203 (2005).
 - [26] D. Heck, G. Schatz, T. Thouw, J. Knapp and J.N. Capdevielle, Technischer Report 6019, Forschungszentrum Karlsruhe, Germany (1998), <http://www-ik.fzk.de/corsika>.
 - [27] D. Chirkin and W. Rhode, hep-ph/0407075v1 (2004).
 - [28] R. Glasstetter et al., in Proc. 26th ICRC, Salt Lake City, USA (1999).
 - [29] J. Hörandel, Astropart. Phys. **19**, 193 (2003).
 - [30] J. Ahrens et al., Nucl. Instrum. Meth. **A524**, 16 (2004).
 - [31] G. Hill and K. Rallins, Astropart. Phys. **19**, 393 (2003).
 - [32] A. Martin, M. Ryskin and A. Stasto, Acta Phys. Polon. **B34**, 3273 (2003).
 - [33] R. Abbasi et al., Phys. Rev. **D84**, 072001 (2011).
 - [34] M. Ackermann *et al.*, J. Geophys. Res. **111** D13203 (2006).
 - [35] D. Chirkin for the IceCube Collaboration, Study of South Pole ice transparency with IceCube flashers, 32nd ICRC proceedings (2011).
 - [36] M. Block, P. Ha, and D. McKay, Phys. Rev. **D82**, 077302 (2010).
 - [37] J. Lundberg, J. Conrad, W. Rolke, and A. Lopez, Comput. Phys. Commun. **181**, 683 (2010).
 - [38] G.J. Feldman and R.D. Cousins, Phys. Rev. **D57**, 3873 (1998).
 - [39] R. Abbasi et al., Astropart. Phys. **34**, 420 (2010).
 - [40] A. V. Avrorin et. al, Astron. Lett. **35**, No. 10, 651 (2009).
 - [41] M. Ackermann et al., Astrophysical Journal **675**, 1014 (2008).
 - [42] R. Abbasi et al., Phys. Rev. **D84**, 082001 (2011).
 - [43] F. W. Stecker, Phys. Rev. **D72**, 107301 (2005).
 - [44] E. Waxman and J. N. Bahcall, Phys. Rev. Lett. **78**, 2292 (1997).